LANGMUIR

Article

Polar−Nonpolar Interfaces of Normal Bicontinuous Cubic Phases in Nonionic Surfactant/Water Systems Are Parallel to the Gyroid Surface

Toshihiko Oka,* Noboru Ohta, and Stephen T. Hyde

Cite This: *Langmuir* 2020, 36, 8687−8694

Read Online

ACCESS | Metrics & More | Article Recommendations | SI Supporting Information

ABSTRACT: We investigated the structures of normal (type I) bicontinuous cubic phases in hexa-, hepta-, and octaethylene glycol dodecyl ether/water mixtures by small-angle X-ray crystallography of single-crystal domains. Reconstructed electron densities showed that the hydrophilic chains with high electron density are confined to a film centered on the surface of the Gyroid (a triply periodic minimal surface), while hydrophobic chains with low electron density are distributed within the pair of interwoven labyrinths carved out by the Gyroid. Further, the local minimum within the high electron density region, due to bulk water, coincides precisely with the Gyroid. This minimum is less pronounced in mixtures with longer ethylene glycol chains, consistent with their decreased water content. Our analysis clearly shows that the polar−nonpolar interfaces are parallel to the Gyroid surface in all mixtures. The repulsive hydration or overlapping force between the pair of facing monolayers of ethylene glycol chains on either side of the Gyroid surface is the likely origin of the parallel interfaces.
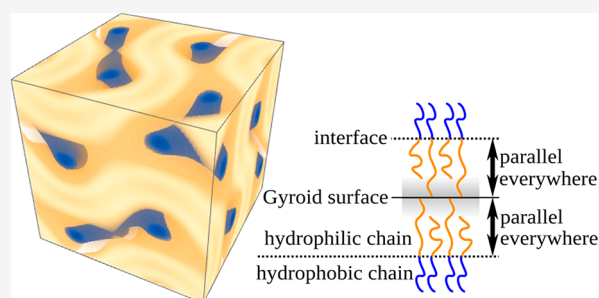
INTRODUCTION

Triply periodic minimal surfaces (TPMSs) extend infinitely in all directions and separate space into two interwoven labyrinths[1] (Figure 1). At any point on a TPMS, the mean curvature (H) is zero while its Gaussian curvature (K) is negative, except at isolated "flat points" (where $K = 0$). TPMSs describe the structures of many different materials both in vivo and in vitro[1] including bicontinuous cubic (Q) phases of lyotropic liquid crystals. These consist of amphiphiles and solvents, such as water and oil, and can adopt various mesophases[2] including two classes of the bicontinuous cubic phases: normal ("type I", Q_I) phases and inverse ("type II", Q_{II}) phase. In the Q_{II} phase, a bilayer of amphiphilic molecules such as lipids is assembled into a curved film following the TPMS.[3,4] Therefore, the TPMS is located within the nonpolar region, and the two interwoven labyrinths are located in the polar region. On the other hand the Q_I is built by an inverse bilayer, folded onto the TPMS. The TPMS is therefore located in the polar region and the labyrinth in the pair of disjoining nonpolar regions.[2] Most studies of the Q_I phase report a geometry related to just one of the TPMSs, Schoen's Gyroid surface.[5] More generally, three distinct Q_{II} phases have been found whose mesostructures are based on the three simplest TPMSs: the P surface (Q_{II}^{229}), the D surface (Q_{II}^{224}), and the Gyroid (Q_{II}^{230}). (Following Luzzati,[6] these are labeled Q_{II}^N, where N is the space group number in the *International Tables for Crystallography*.[7]) X-ray diffraction studies by Luzzati et al. confirmed earlier suggestions[8] that the bilayer membranes of

amphiphilic molecules are located on TPMS in the Q_{II} phases.[9,10]

Amphiphiles, such as lipids and surfactants, are tethered to the polar−nonpolar interfaces, so the loci of those interfaces are important. Among the many analyses of this interfacial structure within the Q_{II} mesophases, two major models have been proposed: one model assumes the interfaces form parallel surfaces to the TPMS (PS model);[1,11] the other model assumes that they form constant mean curvature surfaces (CMCS model).[12,13] The PS model implies that the bilayer film has a constant width, a local condition that would hold, for example, if the energetics of the self-assembly are dominated by the stretching energy of the hydrocarbon chains. On the other hand, the CMCS model leads to stable fluid−fluid interfaces, governed by surface tension and Laplace pressure, since the CMCS model optimizes the interfacial area with respect to arbitrary fluctuations and maintains equal pressure over the interface.[12,14] Our previous small-angle X-ray crystallography analysis revealed that the interfaces within phytantriol−water mixtures forming Q_{II}^{224} and Q_{II}^{230} mesophases are parallel to the TPMS, confirming the PS model.[15]
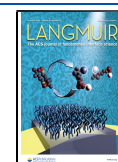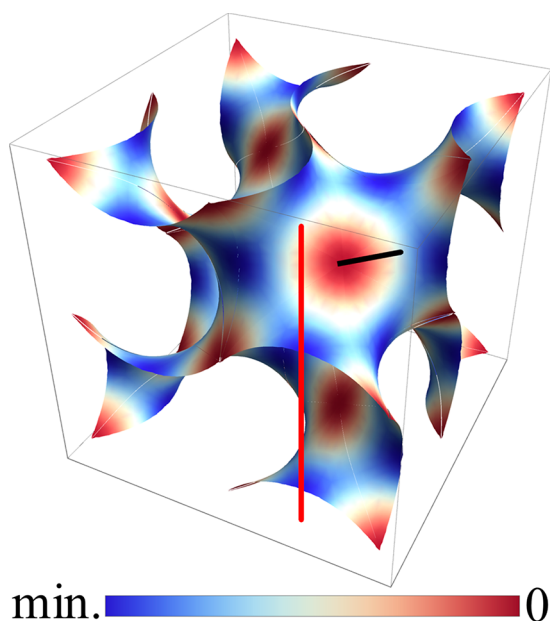
Figure 1. Gyroid TPMS. Colors on the TPMSs indicate Gaussian curvature; red regions are close to zero (flat points), while blue regions are close to minimum negative curvature (saddle points). Colored straight lines are perpendicular to the TPMS at the point of intersection. Black lines, which are parallel to the [111] direction within the cubic lattice, intersect the TPMSs at its flat points, where Gaussian curvatures are zero. Red lines, parallel to the [100] direction, intersect at saddle points, with the most negative Gaussian curvature.

In contrast to Q_{II} mesophases, there are few theoretical or experimental studies on the interface structure of the Q_I phase. In particular, to our knowledge, the interfacial geometry remains unexplored, either theoretically by energy calculations or by observations. Since Q_{II} mesophases are typically formed by amphiphiles whose molecular bulk is dominated by their hydrophobic chains, it is likely that their self-assembly is dictated by the stretching energy of the hydrocarbon chains, resulting in a parallel surface geometry. On the other hand, Q_I mesostructures are adopted by amphiphiles with smaller hydrophobic moieties relative to their hydrophilic volume. Therefore, the free energy contributions of the hydrophilic regions are likely significant. Also, the hydrophobic chains are likely to vary in length, since their packing is dependent on the distribution of distances between the TPMS, the interface, and the related medial surface.[16] The likely geometry of the interfaces within Q_I mesostructures is therefore even more speculative than those within Q_{II} mesostructures. To our knowledge, three-dimensional reconstruction of the electron density map of a lyotropic Q_I mesophase has been reported only for the dodecyltrimethylammonium chloride/water system using the powder X-ray diffraction method.[17] That electron density map revealed low-density domains (comprised of hydrocarbon chains) forming a pair of intertwined labyrinths and the high-density region (containing the polar moiety of the surfactant and water) located in a film centered on the Gyroid. However, the resolution of the structure was low; consequently, many structural details of the Q_I phase remain unknown. For example, the geometry of the polar−nonpolar interface—a key structural feature governing the mesophase stability compared with competing mesostructures—remains unexplored. Here, we recover a more detailed map of the three-dimensional electron density in a Q_I^{230}

mesophase formed by nonionic surfactant−water mixtures via small-angle X-ray crystallography. Also, we demonstrate that, as we found for the Q_{II}^{224} and Q_{II}^{230} mesophases, the polar−nonpolar interface within this Q_I^{230} mesophase is parallel to the Gyroid, as expected from the PS model.

■ MATERIALS AND METHODS

Hexaethylene glycol monododecyl ether ($C_{12}EO_6$), heptaethylene glycol monododecyl ether ($C_{12}EO_7$), and octaethylene glycol dodecyl ether ($C_{12}EO_8$) (purity > 97.0%, Tokyo Chemical Industry Co., Tokyo, Japan) were used without further purification. The Q_I-phase single-crystallization method of $C_{12}EO_6$, $C_{12}EO_7$, and $C_{12}EO_8$ ($C_{12}EO_{6-8}$) is almost the same as that of phytantriol.[15] About 5 μL of distilled water was introduced into a soda glass capillary (Marktube, Hilgenberg GmbH, Germany) with an inner diameter of 1.0 mm; then about 20 mg of $C_{12}EO_{6-8}$ was transferred into the capillary, and it was centrifuged at an acceleration of 600 times of the Earth's gravity for 180 s. The open end of the capillary was sealed with a gas torch. The capillary was incubated at 25 °C for 2−7 days. For small-angle X-ray crystallography, samples with single-crystal regions of more than 5 mm in length were used.

X-ray diffraction was measured at the small-angle X-ray scattering beamline BL40B2 of the synchrotron facility SPring-8 (Hyogo, Japan). The wavelength of the X-rays was set to 0.1000 nm. The full width at half-maximum of the X-ray beam was 0.2 mm in the horizontal direction and 0.2 mm in the vertical direction. Measurements were conducted similarly to those described in previous papers;[18−20] diffraction data was collected from a rotating crystal at room temperature (26 °C). X-ray diffraction from a capillary sample was measured sequentially during a rotation of the sample from 0° to 180°. The exposure time and rotation angle per frame were 0.1 s and 0.1°, respectively. Since the storage ring was operated in the C mode (11 bunch trains × 29), we assume the X-ray intensity was constant. To limit the maximum intensity of the pixel to less than about 10^5 count/s, a copper plate of 40 μm thickness was used as an X-ray attenuator. X-ray diffraction images were indexed and integrated with the XDS program package.[21] The space group of the Q_I^{230} phase ($Ia\bar{3}d$) was already known and assumed for XDS processing.

Analysis of the X-ray data is similar to that described earlier.[15] The electron density in a crystal is obtained by Fourier transformation of the structure factors $F(h)$: $\rho(r) = \sum_h F(h)\exp(-2\pi i r \cdot h)$, where r is a vector in real space and $h = (h\ k\ l)$ is a Miller index. The structure factor can be expressed in terms of its amplitude F and phase α: $F(h) = |F(h)|\exp(i\ \alpha(h)) = F(h)\exp(i\ \alpha(h))$. The diffraction intensity is the square of the structure factor: $I(h) = |F(h)|^2 = (F(h))^2$. Electron density distributions were calculated for the two model mesostructures introduced above. A pair of model mesostructures was built, assuming the interfaces bonding hydrophobic and hydrophilic domains assume the geometries derived from the PS and CMCS models. Models for the electron densities were then reconstructed from those candidate structures. Since the polar surfactant headgroups are tethered closest to the TPMS, both models assume that the water region forms a film centered on the Gyroid TPMS, partially mixed with polar headgroups, and the hydrophobic chains are located away from the TPMS, pointing into the channels. The PS model structure is formed by imposing a constant film thickness for the polar film containing the $C_{12}EO_{6-8}$ headgroups and bulk water. The CMCS model structure contains a CMCS separating polar from hydrophobic moieties, whose mean curvature was tuned by setting the hydrophobic volume fraction to 0.28 (the same as the volume fraction of the hydrophobic region in the final PS model). Both the zero mean curvature Gyoid TPMS and its CMCS were created using Surface Evolver;[22] the CMCS were formed by the method of Shearman et al.[23] Electron densities were assumed to show a steep but continuous change between different regions around interfaces, which are set by the distance from TPMS or CMCS. The model electron density was expressed as the convolution of the step function and a Gaussian to express such distribution. The step functions were set by the distance from the TPMS or CMCS, x. For the PS model, $\rho_{step}^{PS}(x) = \rho_2 U(x -$

$w_1) + (\rho_3 - \rho_2)U(x - w_1 - w_2)$; for the CMCS model, $\rho_{step}^{CMCS}(x) = \rho_2 U(w_2 + x) + (\rho_3 - \rho_2)U(x)$, where $U(x) = 1$ $(x \geq 0)$ or 0 $(x < 0)$, where ρ_2 and ρ_3 are the densities of the hydrophobic and hydrophilic moieties of $C_{12}EO_{6-8}$ and w_1 and w_2 are the thicknesses of the water and hydrophilic domains, respectively. To simplify the functions, the electron density in the water region was set to 0. All locations in the PS mesostructure have positive distance x. In the CMCS model, the magnitude of x measures the shortest distance from a location to the CMCS: $x < 0$ characterizes all polar locations within the volume containing the TPMS, whereas $x > 0$ characterizes distances from points in the nonpolar region to the CMCS. Since the diffraction is essentially sensitive to electron density differences only, the density of the bulk water regions was set to zero. The electron density in each of the $64 \times 64 \times 64$ voxels within a cubic unit cell was calculated accordingly, extended to the liquid crystal mesostructures by aligning the unit cell with sites on the cubic lattice. The resulting models for the Q_I^{230} mesostructure were Fourier transformed and multiplied in reciprocal space with an isotropic three-dimensional Gaussian function, $f_{Gauss}(\mathbf{h}) = \exp(-2\pi^2\sigma^2|\mathbf{h}|^2)$.[20] According to the convolution theorem, a convolution of two functions in real space equals a multiplication in reciprocal space. The Gaussian function represents the structural disorder, imposing random deviation from the ideal crystal lattice. The structural parameters ρ_2, ρ_3, w_1, w_2, and σ in the PS model and ρ_2, ρ_3, w_2, and σ in the CMCS model were optimized to give best fits between expected and measured structure factors in the diffraction patterns, $|F_{exp}(\mathbf{h})|$, by minimizing $\Delta F^2 = \Sigma_h(|F_{exp}(\mathbf{h})| - |F_{model}(\mathbf{h})|)^2$. We used the Nelder−Mead optimization method,[24] which avoids the use of derivatives. So-called R factors are often used in crystallography to quantify the congruence of a model structure with experimental data: the smaller the R factor, the more accurate the structural model. The R factor is defined as $R = \sum_h(||F_{exp}(\mathbf{h})| - k_{scale}|F_{model}(\mathbf{h})||)/|F_{exp}(\mathbf{h})|$. We calculated R factors for the optimized PS and CMCS mesostructures.

The calculation of the electron density, $\rho_{exp}(\mathbf{r})$, was simplified taking into account the space group symmetries[20] (see section 4.7 of *International Tables for X-ray Crystallography*[25]). Amplitudes of the structure factors, $|F_{exp}(\mathbf{h})|$, are the same in the equivalent reflection. Phases, α, of equivalent reflections have different signs in some conditions of $Ia\bar{3}d$ symmetry.[25] The phases α were determined from the Fourier transformations of the model data as described in the Results and Discussion section.

RESULTS AND DISCUSSION

Phase diagrams of $C_{12}EO_{6-8}$−water mixtures have been reported by several groups.[26−28] All phase diagrams report a Q_I mesophase located in a narrow concentration window between the hexagonal H_I phase and the lamellar L_α phase at 25 °C. $C_{12}EO_{6-8}$ and water were placed adjacent to each other in a capillary tube at room temperature. Since pure $C_{12}EO_{6-8}$ is a L_1 mesophase at ambient conditions, mutual diffusion resulted in the formation of H_I, Q_I, and L_α mesophases along the length of the capillary (Figure 2b and 2c). These phases were distinguished optically: the L_α and H_I phases exhibit birefringence, but the Q_I phase does not. Those phase identifications were confirmed by X-ray diffraction. Remarkably, Q_I mesophases formed by this method were often single crystals (Figure S1). Growth of single crystals of $C_{12}EO_6$ Q_I phases in capillaries has been reported previously, though they required a duration of several months to grow the single-crystal domain in a capillary.[29] Our diffusion method required no more than 1 week. (We note that single crystals of a Q_{II} mesophase were formed similarly in phytantriol−water mixtures.[15])

As described above, X-ray diffraction images of single-crystal domains formed by our diffusion method were collected by the rotating crystal method[15,20] and processed with the XDS program package.[21] The resulting normalized amplitudes of
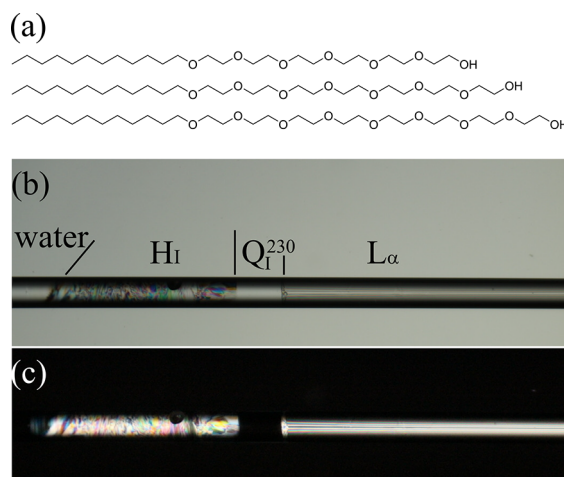

Figure 2. (a) Molecular structures of $C_{12}EO_6$, $C_{12}EO_7$, and $C_{12}EO_8$. (b and c) Close-up of a capillary sample after 4 days. Sample placed between two parallel (b) and orthogonal (c) polarizing plates. Diameter of the capillary was about 1.0 mm.

the structural factors are shown in Figures 3 and S2 and Table S1: corresponding reflections in $C_{12}EO_6$, $C_{12}EO_7$, and $C_{12}EO_8$
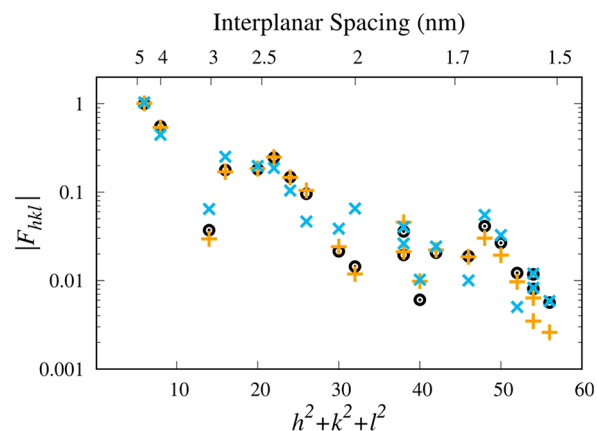

Figure 3. Amplitudes of structure factors, $|F_{hkl}|$, of $C_{12}EO_6$. $(h\ k\ l)$ are Miller indices of a reflection; black circles are amplitudes determined by X-ray diffraction measurements; orange pluses and sky-blue crosses are amplitudes calculated from parallel surface (PS) and constant mean curvature surface (CMCS) models, respectively.

had very similar amplitudes. Both mesostructures are therefore very similar. Next, we built optimized PS and CMCS model mesostructures that best recovered these structure factors. The PS and CMCS models were created by a convolution of a three-dimensional isotropic Gaussian function and discrete electron densities depending on the distances from the polar−nonpolar interfaces, as described in the Materials and Methods section. Results are collected in Figure 3 (with further data in Figure S2 and Table S2). Figure 3 shows the amplitudes of the structure factors for both model mesostructures. The PS model fits the experimental data well, with R factors of 0.046, 0.036, and 0.032 for $C_{12}EO_6-$, $C_{12}EO_7-$, and $C_{12}EO_8-$water mixtures, respectively. On the other hand, the CMCS model has some deviations from the experimental data (e.g., an R factor of 0.190 for $C_{12}EO_6$ water mixtures).

Recall from the discussion above that estimation of the three-dimensional electron density distributions requires knowledge of the phase factors, $\alpha(\mathbf{h})$. They cannot be

obtained directly from the X-ray intensity data; however, the diffraction confirms the centrosymmetric space group for all $C_{12}EO_{6-8}$ mesophases, so these phases must be either 0 or π. They were inferred by generating electron density distributions for the PS and CMCS models with phase factors that gave an optimized fit to the experimental data of $C_{12}EO_6$. In fact, both models were optimized by the same phase factors, since differences between the mesostructures of the optimized PS and CMCS models were small. Further, the phase factors for optimized PS model mesostructures of $C_{12}EO_7$ and $C_{12}EO_8$ were the same (Table S1), also due to the small structural differences between $C_{12}EO_{6-8}$ mesophases. The electron density was then calculated using these phases along with structure factor amplitudes obtained from the experiment (Figure 4). The polar part of $C_{12}EO_{6-8}$ with high electron density is located on the Gyroid, and the nonpolar region with lower electron density is located toward the center of two interwoven networks separated by the Gyroid (Figure 4d). That narrow local minimum in the high-electron density regions is consistent with the presence of a thin bulk water region, sandwiched between opposing ethylene glycol (ethylene oxide, EO) chain monolayers of $C_{12}EO_{6-8}$ on the Gyroid. $C_{12}EO_6$ has a short EO chain, and the water content of $C_{12}EO_6$ Q_I phase is high, so the minimum is more pronounced (Figure 4a). On the other hand, since $C_{12}EO_8$ has a long EO chain and the water content is low, the minimum is less defined and shallower (Figure 4c).

The PS and CMCS have been used as interface structure models in the study of the Q phases of lyotropic liquid crystals.[12,30] Therefore, it is important to determine if the two models can be distinguished experimentally via the electron density distribution and, if so, which model better describes the data. Figure 5 shows planar sections of the PS and CMCS models of $C_{12}EO_6$. There are clear differences in the two models, namely, the presence of the narrow local minimum of the polar region mentioned in the previous paragraph and the shapes of the (blue-colored) low-density regions. The PS model agrees well with the electron density map obtained from the experimental diffraction data, shown in Figure 4a. On the other hand, the CMCS model is less faithful to the experimental data. Since the phases of the structure factors of the two models are the same, differences in the electron density distributions are due to amplitudes only.

The electron density distributions along axes normal to the Gyroid, passing through the flat and (most negatively curved) saddle points, are shown in Figure 6. The distributions estimated for the PS model mesostructure are in good agreement with the experimental data. The CMCS models give a polar region (with high electron density) which is narrower at the flat point than the experimental data. That discrepancy is not seen in the PS model. Further, the distinct local minimum of density at the center of the polar region reconstructed from the data and seen in the PS model is absent in the CMCS model (Figure 6b). The water region is particularly thin at the flat point, so the polar EO chains of the opposing $C_{12}EO_6$ monolayers are very close to each other in the CMCS model (Figure 7). The polar volume defined by the CMCS model is thickest at the saddle points of the Gyroid, where the Gaussian curvature of the TPMS is most negative (|K| maximal), and thinnest at flat points (|K| minimal)[31] as shown in Figure 6. This dependence of the thickness of the polar region on the Gaussian curvature and therefore the location on the TPMS is inconsistent with the experimental
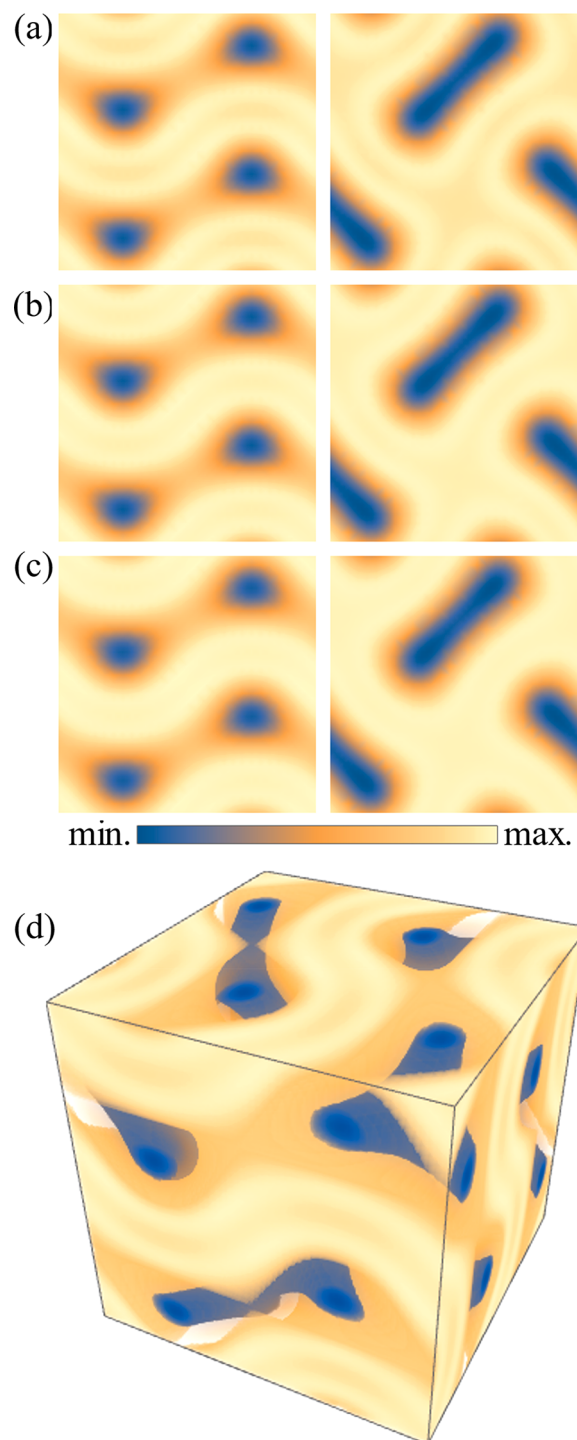

Figure 4. Two-dimensional electron density maps based on experimental data of a single (conventional cubic) unit cell, sliced at $x = 0$, and $0.125a$ (from left to right, where a is the lattice constant) of (a) $C_{12}EO_6$, (b) $C_{12}EO_7$, and (c) $C_{12}EO_8$. (d) Three-dimensional electron densities of $C_{12}EO_6$ within the unit cell. Intermediate electron density regions (from -2 to 0) are transparent for visibility.

data. This inconsistency is not seen in the PS model. Similarly, the PS models of the $C_{12}EO_7$ and $C_{12}EO_8$ electron density distributions are also in good agreement with experimental data (Figure S3).

Our analysis therefore supports the PS models within the Q_I mesophase with strictly parallel interfaces equidistant from a Gyroid midsurface. Previously, we showed that the interfaces
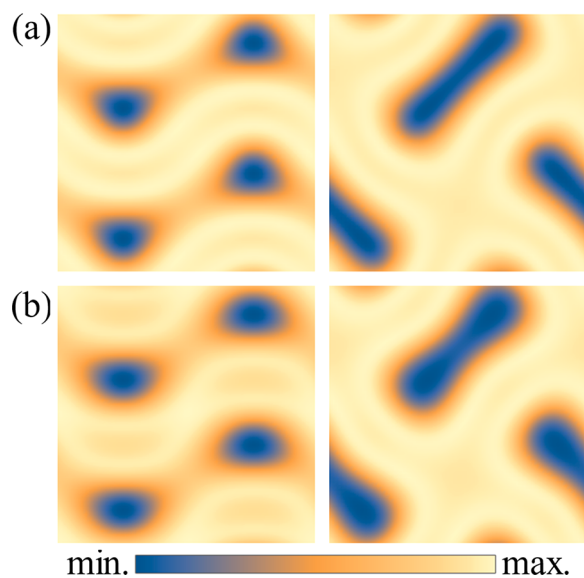
Figure 5. Two-dimensional electron density maps of a single (conventional cubic) unit cell, sliced at $x = 0$, and $0.125a$ (from left to right, where a is the lattice constant) in $C_{12}EO_6$ unit cells of the (a) parallel surface model and (b) constant mean curvature surface model.
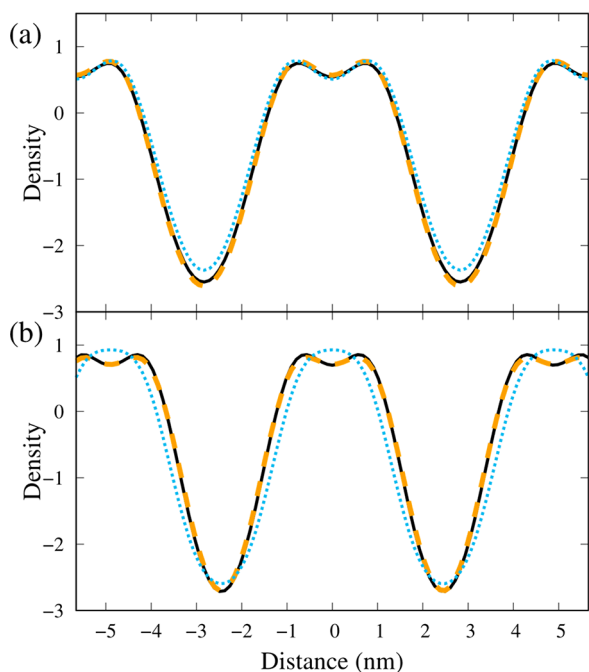

Figure 6. One-dimensional electron density distributions along straight lines corresponding to those in Figure 1 for $C_{12}EO_6$. Lines follow the [100] direction in a and [111] in b. Distance from the Gyroid is mapped on the horizontal axis. Black solid lines describe the density distributions from experimental data, while orange dashed and sky-blue dotted lines are parallel surface and constant mean curvature surface models, respectively.

within the Q_{II}-phase mesostructures in phytantriol/water systems are also parallel to TPMS.[15] In the Q_{II} phase, the nonpolar molecular moieties are located within the single continuous volume defined by the pair of interfaces containing the TPMS and the polar moieties of the amphiphile occupy the remaining volumes. Therefore, only hydrophobic chains of
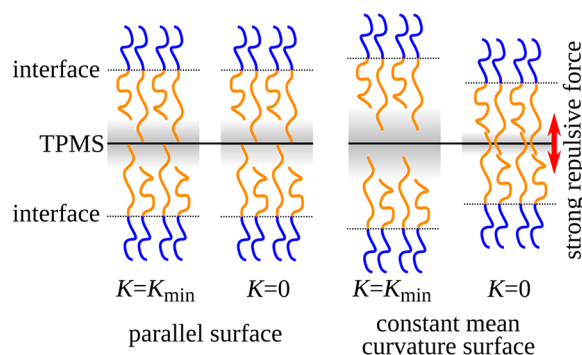

Figure 7. Cartoon explaining the origin of the parallel polar−nonpolar interfaces in Q_I mesophases. PS model mesostructure is characterized by equal spacings between facing headgroup chains everywhere, so repulsive forces are constant regardless of positions. In contrast, within the CMCS model mesostructure, at the umbilic on the CMCS (corresponding to the flat point on the TPMS), the force is strongly repulsive, since the spacing between facing headgroup chains is close. CMCS model therefore forms a less stable mesostructure than that of the PS model. Blue lines describe hydrophobic chains of the amphiphile, orange lines hydrophilic headgroup chains, and gray region the bulk water domain. (In Q_{II} mesostructres, the blue lines describe polar headgroup moieties of the amphiphile, the orange lines hydrophobic chains, and the gray area bulk oil area.)

phytantriol occupy the TPMS volume, and the midplane of the bilayer is located on the TPMS. In that case, we concluded that the stretching energy of the hydrocarbon chains dominated the assembly, and parallel interfaces, with constant chain length, resulted in minimizing that energy.[14] Indeed, theoretical calculations, which assume the hydrocarbon chain are ideal Gaussian chains, showed that the constant chain length is energetically favorable in the Q_{II} mesophase.[32] In the Q_I phase, the molecular environment is different: the polar moieties (comprising the hydrophilic EO chains of the surfactant molecules and water) are located within the film containing the TPMS. The surfactant is tethered to the interfaces, but water molecules have no positional restriction. The presence of water would therefore be expected to increase the flexibility of the Q_I mesostructure in the polar region. However, that flexibility may be negated by a compensating repulsive force between the monolayers of hydrophilic chains. Lyle and Tidy observed a repulsive force between the EO chains of the opposing monolayer of the $C_{12}EO_4$/water system,[33] likely due to hydration[33] or overlap[34] of the opposed EO chains. The magnitude of the repulsive force can be estimated by the Alexander−de Gennes theory

$$P \approx \left[\left(\frac{2L}{D} \right)^{9/4} - \left(\frac{D}{2L} \right)^{3/4} \right]$$

for $D < 2L$, where D is the distance between the interfaces and L is the length of the hydrophilic chain.[34−36] That repulsive overlap force is again due to the entropic behavior of (Gaussian) molecular chains.[35,36] The same repulsive force likely acts between the opposing EO chain layers of $C_{12}EO_{6-8}$ in the systems under study here, since this repulsive force is common in nonionic surfactant layers.[37] The free energy contribution from that repulsive force is minimized for constant distances between opposed monolayers. As a result, the PS model, whose distance between the opposing EO chain layers is constant, is energetically favored over the CMCS model, which requires variable distances. In summary, the

entropic requirements of molecular chains induce parallel interfaces in both Q_I and Q_{II} mesophases. In the Q_I mesophases of the $C_{12}EO_{6-8}$ case that induced an effective repulsive interaction between the facing EO chain layers on either side of the TPMS.[33,34] For similar reasons, it is likely that the polar−nonpolar interfaces are also parallel to the Gyroid in Q_I mesophases containing many other nonionic surfactants. Therefore, in both the Q_I and the Q_{II} mesophases, an entropic repulsive force of the molecular chains on TPMS determines the interfacial mesostrucutre. We predict that whenever a repulsive interaction is strong in these Q mesophases, the interface will be parallel to the TPMS, regardless of the mesophase type.

The electron density maps of $C_{12}EO_{6-8}$ show differences in the water regions (Figure 4). The shorter the EO chain, the clearer the water region. Although the exact amount of water cannot be determined from our experiments, in the phase diagram of $C_{12}EO_{6-8}$ the Q_I phase appears in a more (water) dilute region, as the EO chain is shorter.[26,28] Since the polar−nonpolar interface is a parallel surface, the volume fraction of the polar (or nonpolar) region is determined from the interface area per unit volume.[38,39] The area per molecule at the polar−nonpolar interface is likely to be similar, since the $C_{12}EO_{6-8}$ molecular structure differs only in the EO chain. The lattice constants of $C_{12}EO_{6-8}$ Q_I phases are almost the same (Table S1); therefore, the volume fractions in the polar regions of $C_{12}EO_{6-8}$ are approximately equal, and differences in water volumes compensate for the volume differences in EO chains. On the other hand, the lattice constants depend somewhat on the length of the EO chains: the lattice constant reduces as the EO chain extends (Table S1). The longer the EO chain, the greater the repulsive force between adjacent molecules and the slightly larger interfacial area per molecule. Increasing the interfacial area per molecule decreases the lattice constant and lowers the volume fraction of the polar region.[26,28]

A striking feature of these Q_I mesophases is the absence of the additional bicontinuous mesophases related to the P and D TPMS, i.e., Q_I^{229} and Q_I^{224}. (In type II systems, three distinct mesophases, Q_{II}^{230}, Q_{II}^{229}, and Q_{II}^{224} are typically formed.) The formation of just one type I mesophase, Q_I^{230}, may be explained as follows. In the Q_I mesostructure, nonpolar hydrocarbon chains are assembled within the pair of interwoven labyrinths with one end tethered to the (parallel) interfaces. Assuming that the hydrocarbon chains extend, on average, normally outward from the interfaces in the PS model, the free polar chain end is ideally located on the medial surface, giving void-free domains. The radial distance between the hyperbolic interfaces and the medial surfaces necessarily varies depending on the location on the interface and the particular underlying TPMS describing the interfaces.[16] Note that the global geometry of the Gyroid TPMS enforces the *total* radial distance from the TPMS to the medial surface. In contrast to (for example) a spherical interface, total distances are not constant but vary from point to point on the TPMS. That variation is narrowest for the Gyroid, followed by the D and P surfaces.[16] Since the total distance is the sum of the polar and nonpolar distances and the PS model imposes constant polar width for type I systems, nonpolar radial distances must vary. Also, those variations are minimized in the Q_I^{230} mesophase, based on the Gyroid TPMS. Those global geometric differences between the P, the D, and the Gyroid therefore affect the stability of the hydrocarbon chain packing, since a single radial distance is preferred, corresponding to the relaxed

chain length of molten hydrocarbon chains. The Gyroid mesostructure is therefore the most favored pattern, while the D and (to a much larger degree) P structures incur a larger free energy cost. This effect may explain the absence of known Q_I mesophases adopting the P and D structures.

It is worth reiterating that the nonpolar volumes available to each chain are necessarily *globally* inhomogeneous, since the axial distances vary even in the Gyroid mesostructure in the PS model. (Global homogeneity refers to the chain packing variations due to differences between opposed interfaces rather than local homogeneity, which is induced by curvature variations.[16]) That source of energetic frustration disfavors the PS model, since those inhomogeneities within the nonpolar domains are induced to allow homogeneity of the polar volume available to each polar domain per surfactant molecule, comprising a (hydrophilic) chain and water. This paradox suggests that the repulsive forces between opposed EO chains are stronger than analogous repulsions between opposed nonpolar hydrocarbon chains. Consequently, the nonpolar hydrocarbon moieties are therefore predicted to be softer than the polar moieties. The underlying physics for this remains unclear, though this feature is not unreasonable, since (i) the EO chains are longer than their nonpolar hydrocarbon counterparts and (ii) the presence of bulk water may further stiffen the polar domain.

In the phase diagrams of $C_{12}EO_{6-8}$−water mixtures the Q_I phase appears in a narrow region between the (low water fraction) L_α phase and the (high water) H_I phase.[26−28] The idealized H_I mesostructure consists of a regular 2-periodic array of cylindrical micelles packed with *p6mm* plane symmetry. For a fixed water fraction, the minimum distance between the interfaces across the polar regions is shorter in the H_I mesostructure than that of the Q_I mesostructure, assuming the micelles in the H_I mesostructure are cylinders with a circular cross-section. In that case, the repulsive overlapping force between EO chains within adjacent cylindrical micelles is larger in this model H_I mesostructure than the analogous repulsion in the Q_I mesostructure. If the overlapping force between cylindrical micelles is large in the H_I phase and the hydrocarbon chain region is soft, the interfacial geometry in the H_I mesostructure may deviate from an idealized circular cross-section, so a better comparison of energies within these competing mesophases should include that possibility. Irrespective of the details of those deviations, as the water content increases, the repulsive force is weakened and hence the appearance of the H_I mesophase under more dilute conditions. Further, the Q_I phase is absent in the phase diagrams of some surfactant/water systems.[40,41] This absence suggests that, in those systems, repulsive interactions between opposed polar groups contribute less to the free energy of the system than the hydrocarbon chain contributions, which imposes a preferred chain length, and therefore a fixed nonpolar radial distance, disfavoring the TPMS structures.

■ CONCLUSION

In summary, we determined the three-dimensional electron density map within the Q_I mesophases of $C_{12}EO_{6-8}$−water mixtures by small-angle X-ray crystallography of single-crystal domains. The $C_{12}EO_{6-8}$ polar headgroup moieties, with high electron density, were located adjacent to the Gyroid, and the nonpolar chains, with low density, were localized within the pair of interwoven labyrinths to either side of the Gyroid. A local minimum of electron density was located in a film of

constant thickness, centered precisely on the Gyroid, within the high electron density region. Our analysis showed that this minimum defines the bulk water domain. In addition, a model mesostructure, whose polar−nonpolar interfaces are parallel to the Gyroid (the PS model), was consistent with the data, in contrast to a model assuming the CMCS. We showed previously that the interfaces within the Q_{II} mesostructures in phytantriol−water mixtures were also parallel to the corresponding TPMS.[15] Therefore, both the Q_I and the Q_{II} mesophases are characterized by parallel interfaces, themselves parallel to a TPMS. The likely cause of this parallel geometry in all of these systems is the entropic behavior of hydrophilic (Q_I) or hydrophobic (Q_{II}) chains.

■ ASSOCIATED CONTENT

Ⓢ Supporting Information

The Supporting Information is available free of charge at https://pubs.acs.org/doi/10.1021/acs.langmuir.0c00597.

> Amplitudes of structure factors, phases, lattice constants and optimized parameters of model functions, X-ray diffraction images, one-dimensional electron density distributions (PDF)

■ AUTHOR INFORMATION

Corresponding Author

Toshihiko Oka − *Department of Physics, Faculty of Science and Nanomaterials Research Division, Research Institute of Electronics, Shizuoka University, Shizuoka 422-8529, Japan;* ⓞ orcid.org/0000-0002-1676-9231; Email: oka.toshihiko@ shizuoka.ac.jp

Authors

Noboru Ohta − *SPring-8/JASRI, Sayo-gun, Hyogo 679-5198, Japan*

Stephen T. Hyde − *Department of Applied Mathematics, Research School of Physics and Engineering, Australian National University, Canberra, Australian Capital Territory 2601, Australia; School of Chemistry, University of Sydney, New South Wales 2006, Australia*

Complete contact information is available at:
https://pubs.acs.org/10.1021/acs.langmuir.0c00597

Notes

The authors declare no competing financial interest.

■ ACKNOWLEDGMENTS

■ REFERENCES

(1) Hyde, S.; Blum, Z.; Landh, T.; Lidin, S.; Ninham, B. W.; Andersson, S.; Larsson, K. *The Language of Shape: The Role of Curvature in Condensed Matter: Physics, Chemistry and Biology*; Elsevier, 1996.

(2) Hyde, S. T. Identification of Lyotropic Liquid Crystalline Mesophases. *Handbook of Applied Surface and Colloid Chemistry*; J. Wiley & Sons, 2002; Vol. 16, pp 299−332.

(3) Seddon, J. M.; Templer, R. H. Polymorphism of Lipid-Water Systems. *Structure and Dynamics of Membranes*; North-Holland, 1995; Vol. 1, pp 97−160.

(4) Yamazaki, M. Transformation Between Liposomes and Cubic Phases of Biological Lipid Membranes Induced by Modulation of Electrostatic Interactions. *Advances in Planar Lipid Bilayers and Liposomes*; Academic Press, 2009; Vol. 9, pp 163−209.

(5) Schoen, A. H. Infinite Periodic Minimal Surfaces without Self-Intersections; *NASA Technical Note 05541*; NASA, 1970.

(6) Luzzati, V.; Mariani, P.; Gulik-Krzywicki, T. The Cubic Phases of Liquid-Containing Systems: Physical Structure and Biological Implications. *Physics of Amphiphilic Layers*; Springer Proceedings in Physics; Springer: Berlin, Heidelberg, 1987; pp 131−137.

(7) In *International Tables for Crystallography*, 5th ed.; Hahn, T., Ed.; Springer: Dordrecht, 2002; Vol. A.

(8) Hyde, S. T.; Andersson, S.; Ericsson, B.; Larsson, K. A Cubic Structure Consisting of a Lipid Bilayer Forming an Infinite Periodic Minimum Surface of the Gyroid Type in the Glycerolmonooleat-Water System. *Z. Für Krist. - Cryst. Mater.* **1984**, *168* (1−4), 213−220.

(9) Mariani, P.; Luzzati, V.; Delacroix, H. Cubic Phases of Lipid-Containing Systems: Structure Analysis and Biological Implications. *J. Mol. Biol.* **1988**, *204* (1), 165−189.

(10) Luzzati, V.; Vargas, R.; Mariani, P.; Gulik, A.; Delacroix, H. Cubic Phases of Lipid-Containing Systems: Elements of a Theory and Biological Connotations. *J. Mol. Biol.* **1993**, *229* (2), 540−551.

(11) Hyde, S. T. Swelling and Structure. Analysis of the Topology and Geometry of Lamellar and Sponge Lyotropic Mesophases. *Langmuir* **1997**, *13* (4), 842−851.

(12) Anderson, D. M.; Gruner, S. M.; Leibler, S. Geometrical Aspects of the Frustration in the Cubic Phases of Lyotropic Liquid Crystals. *Proc. Natl. Acad. Sci. U. S. A.* **1988**, *85* (15), 5364−5368.

(13) Templer, R. H. Thermodynamic and Theoretical Aspects of Cubic Mesophases in Nature and Biological Amphiphiles. *Curr. Opin. Colloid Interface Sci.* **1998**, *3* (3), 255−263.

(14) Chen, H.; Jin, C. Competition Brings out the Best: Modelling the Frustration between Curvature Energy and Chain Stretching Energy of Lyotropic Liquid Crystals in Bicontinuous Cubic Phases. *Interface Focus* **2017**, *7* (4), 20160114.

(15) Oka, T.; Ohta, N.; Hyde, S. Polar−Nonpolar Interfaces of Inverse Bicontinuous Cubic Phases in Phytantriol/Water System Are Parallel to Triply Periodic Minimal Surfaces. *Langmuir* **2018**, *34* (50), 15462−15469.

(16) Schröder, G. E.; Ramsden, S. J.; Christy, A. G.; Hyde, S. T. Medial Surfaces of Hyperbolic Structures. *Eur. Phys. J. B* **2003**, *35* (4), 551−564.

(17) Mariani, P.; Amaral, L. Q.; Saturni, L.; Delacroix, H. Hexagonal-Cubic Phase Transitions in Lipid Containing Systems: Epitaxial Relationships and Cylinder Growth. *J. Phys. II* **1994**, *4* (8), 1393−1416.

(18) Oka, T. Transformation between Inverse Bicontinuous Cubic Phases of a Lipid from Diamond to Primitive. *Langmuir* **2015**, *31* (10), 3180−3185.

(19) Oka, T. Transformation between Inverse Bicontinuous Cubic Phases of a Lipid from Diamond to Gyroid. *Langmuir* **2015**, *31* (41), 11353−11359.

(20) Oka, T. Small-Angle X-Ray Crystallography on Single-Crystal Regions of Inverse Bicontinuous Cubic Phases: Lipid Bilayer Structures and Gaussian Curvature-Dependent Fluctuations. *J. Phys. Chem. B* **2017**, *121* (50), 11399−11409.

(21) Kabsch, W. XDS. *Acta Crystallogr., Sect. D: Biol. Crystallogr.* **2010**, *66* (2), 125−132.

(22) Brakke, K. A. The Surface Evolver. *Exp. Math.* **1992**, *1* (2), 141−165.

(23) Shearman, G. C.; Khoo, B. J.; Motherwell, M.-L.; Brakke, K. A.; Ces, O.; Conn, C. E.; Seddon, J. M.; Templer, R. H. Calculations of

and Evidence for Chain Packing Stress in Inverse Lyotropic Bicontinuous Cubic Phases. *Langmuir* **2007**, *23* (13), 7276−7285.

(24) Press, W. H.; Flannery, B. P.; Teukolsky, S. A.; Vetterling, W. T. *Numerical Recipes in C: The Art of Scientific Computing*, 2nd ed.; Cambridge University Press: Cambridge, New York, 1992.

(25) Henry, N. F. M.; Lonsdale, K. *International Tables for X-Ray Crystallography*; Kynoch Press: Birmingham, England, 1969; Vol *1*.

(26) Mitchell, D. J.; Tiddy, G. J. T.; Waring, L.; Bostock, T.; McDonald, M. P. Phase Behaviour of Polyoxyethylene Surfactants with Water. Mesophase Structures and Partial Miscibility (Cloud Points). *J. Chem. Soc., Faraday Trans. 1* **1983**, *79* (4), 975−1000.

(27) Conroy, J. P.; Hall, C.; Leng, C. A.; Rendall, K.; Tiddy, G. J. T.; Walsh, J.; Lindblom, G. Nonionic Surfactant Phase Behavior. The Effect of CH_3 Capping of the Terminal OH. Accurate Measurements of Cloud Curves. In *Surfactants and Macromolecules: Self-Assembly at Interfaces and in Bulk*; Lindman, B., Rosenholm, J. B., Stenius, P., Eds.; Progress in Colloid & Polymer Science; Springer, 1990; pp 253−262.

(28) Huang, K. L.; Shigeta, K.; Kunieda, H. Phase Behavior of Polyoxyethylene Dodecyl Ether-Water Systems. *Trends in Colloid and Interface Science XII*; Progress in Colloid & Polymer Science; Springer, 1998; pp 171−174.

(29) Rançon, Y.; Charvolin, J. Displacement Disorder in a Liquid Crystalline Phase with Cubic Symmetry. *J. Phys. (Paris)* **1987**, *48* (6), 1067−1073.

(30) Templer, R. H.; Seddon, J. M.; Duesing, P. M.; Winter, R.; Erbes, J. Modeling the Phase Behavior of the Inverse Hexagonal and Inverse Bicontinuous Cubic Phases in 2:1 Fatty Acid/Phosphatidyl-choline Mixtures. *J. Phys. Chem. B* **1998**, *102* (37), 7262−7271.

(31) Große-Brauckmann, K. Gyroids of Constant Mean Curvature. *Exp. Math.* **1997**, *6* (1), 33−50.

(32) Schwarz, U. S.; Gompper, G. Bending Frustration of Lipid−Water Mesophases Based on Cubic Minimal Surfaces. *Langmuir* **2001**, *17* (7), 2084−2096.

(33) Lyle, I. G.; Tiddy, G. J. T. Hydration Forces between Surfactant Bilayers: An Equilibrium Binding Description. *Chem. Phys. Lett.* **1986**, *124* (5), 432−436.

(34) Israelachvili, J. N.; Wennerstroem, H. Entropic Forces between Amphiphilic Surfaces in Liquids. *J. Phys. Chem.* **1992**, *96* (2), 520−531.

(35) de Gennes, P. G. Polymers at an Interface; a Simplified View. *Adv. Colloid Interface Sci.* **1987**, *27* (3), 189−209.

(36) Israelachvili, J. N. *Intermolecular and Surface Forces*, Revised 3rd ed.; Academic Press, 2011.

(37) Claesson, P. M.; Kjellin, M.; Rojas, O. J.; Stubenrauch, C. Short-Range Interactions between Non-Ionic Surfactant Layers. *Phys. Chem. Chem. Phys.* **2006**, *8* (47), 5501−5514.

(38) Engblom, J.; Hyde, S. T. On the Swelling of Bicontinuous Lyotropic Mesophases. *J. Phys. II* **1995**, *5* (1), 171−190.

(39) Turner, D. R.; Wang, Z.-G.; Gruner, S.; Mannock, D.; Mcelhaney, R. Structural Study of the Inverted Cubic Phases of Di-Dodecyl Alkyl-*β*-D-Glucopyranosyl-Rac-Glycerol. *J. Phys. II* **1992**, *2* (11), 2039−2063.

(40) Eriksson, P. O.; Lindblom, G.; Arvidson, G. NMR Studies of Micellar Aggregates in 1-Acyl-Sn-Glycerophosphocholine Systems. The Formation of a Cubic Liquid Crystalline Phase. *J. Phys. Chem.* **1987**, *91* (4), 846−853.

(41) Blin, J. L.; Lesieur, P.; Stébé, M. J. Nonionic Fluorinated Surfactant: Investigation of Phase Diagram and Preparation of Ordered Mesoporous Materials. *Langmuir* **2004**, *20* (2), 491−498.